Geological and geochemical constraints on the origin of the Early Cambrian Kalaizi Fe–Ba deposit in Western Kunlun, NW China

Zheng, Mengtian; Wang, Changle; Zhang, Lianchang; Shi, Zongbo; Zhu, Mingtian; Li, Zhiquan; He, Lidong

DOI:
10.1016/j.oregeorev.2017.09.025

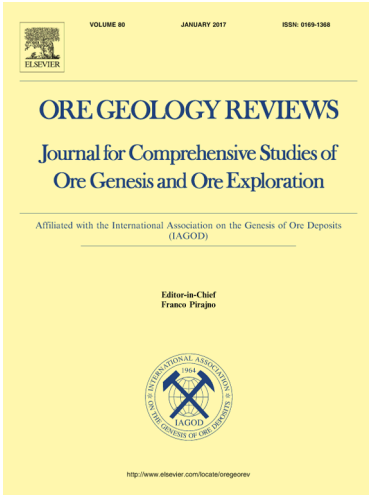

Geological and geochemical constraints on the origin of the Early Cambrian Kalaizi Fe–Ba deposit in Western Kunlun, NW China

Mengtian Zheng, Changle Wang, Lianchang Zhang, Zongbo Shi, Mingtian Zhu, Zhiquan Li, Lidong He

PII: S0169-1368(16)30348-1
DOI: https://doi.org/10.1016/j.oregeorev.2017.09.025
Reference: OREGEO 2374

To appear in: *Ore Geology Reviews*

Received Date: 20 June 2016
Revised Date: 18 September 2017
Accepted Date: 23 September 2017

Please cite this article as: M. Zheng, C. Wang, L. Zhang, Z. Shi, M. Zhu, Z. Li, L. He, Geological and geochemical constraints on the origin of the Early Cambrian Kalaizi Fe–Ba deposit in Western Kunlun, NW China, *Ore Geology Reviews* (2017), doi: https://doi.org/10.1016/j.oregeorev.2017.09.025

Geological and geochemical constraints on the origin of the Early Cambrian Kalaizi Fe–Ba deposit in Western Kunlun, NW China

Mengtian Zheng[a,b], Changle Wang[a], Lianchang Zhang[a,*], Zongbo Shi[c], Mingtian Zhu[a], Zhiquan Li[a], Lidong He[d]

[a] Key laboratory of Mineral Resources, Institute of Geology and Geophysics, Chinese Academy of Sciences, Beijing 100029, China

[b] University of Chinese Academy of Sciences, Beijing 100049, China

[c] School of Geography Earth and Environmental Sciences, University of Birmingham, Birmingham, UK

[d] No. 2 Geological Party, Xinjiang Bureau of Geology and Mineral Resources, Kashigar 844002, China

* Corresponding author. Tel: +86 10 82998185; fax: +86 10 62010846

Email address: lczhang@mail.iggcas.ac.cn (L. Zhang)

Abstract: The Kalaizi deposit in the Bulunkuole Group of Taxkorgan area, Western Kunlun (NW China) is a unique regional Fe–Ba deposit accompanied with sporadic Fe–Pb–Zn sulfide mineralization within a series of iron deposits. All the ore bodies are stratabound and hosted by the Early Cambrian metamorphosed argillaceous clastic rocks. Here, we analyzed C–S–O–Sr isotopes and trace elements in individual minerals (e.g., magnetite, barite, ankerite) from the Kalaizi deposit to investigate the origin of this deposit for the first time. The S isotope fractionation (average of 21‰) between sulfate and sulfide minerals provided clear evidence that the deposit was formed in a semi-closed marine depositional environment with moderate replenishment of seawater sulfate. The distinct Post-Archean Australian Shale (PAAS)-normalized positive Eu anomalies (2.02 to 11.03) and lower Y/Ho ratios (27.2 to 33.4) relative to modern seawater in all individual magnetite minerals separated from magnetite–barite ores and the $\delta^{18}O$ isotope signatures (10.0 to 13.0‰) in individual sulfate minerals suggested that hydrothermal activity played an

important role in the formation of the deposit. Barium was likely derived from the dissolution of marine barite with a contribution from more radiogenic terrigenous sediments considering the slight deviations (within ±0.0013) of $^{87}Sr/^{86}Sr$ ratios of Kalaizi barites from the Early Cambrian seawater. The sulfate and sulfide minerals in the ore deposit should evolve from coeval seawater containing residual SO_4^{2-} and resultant H_2S by means of bacterial sulfate reduction process because (i) $\delta^{34}S$ values (37.8 to 42.8‰) of anhydrite and barite minerals were slightly higher than those of penecontemporaneous seawater, (ii) pyrite and galena minerals owned $\delta^{34}S$ values (16.3 to 23.5‰) were lower than coeval seawater, and (iii) ^{13}C isotope values (-10.0 to -12.1‰) of single ankerite minerals were depleted. To summarize, the Kalaizi bedded Fe–Ba deposit is interpreted as a cold seep barite deposit overprinted by hydrothermal fluids.

Key words: magnetite, barite, hydrothermal fluid, cold seep origin, Taxkorgan

1. Introduction

Sediment-hosted stratiform barite, commonly formed through the mixing of Ba-bearing fluids leaching from silicate minerals with sulfate-rich marine water (Hanor, 2000), accounts as the main source of industrial barite. Most of these barite deposits have been found in South China, the Qingling Mountains of central China (Wang and Li, 1991; Xu et al., 2016), Nevada in the Western US and Mangampeta in India (Clark et al., 2004; Maynard and Okita, 1991). Research on the origin of stratiform barite provides important information on the study of paleoceanography, paleotectonics, and economic geology (Torres et al., 2003). An understanding of key features of modern sedimentary barite is a prerequisite for identifying the origin of ancient barite deposits (Torres et al, 2003; Johnson et al., 2004, 2009; Canet et al., 2014). In general, the genetic types of modern sedimentary barite can be divided into four subtypes: (1) marine barite, which precipitates directly from seawater in the presence of decaying organic debris (Dehairs et al., 1980; Bishop, 1988) and records

seawater productivity and chemistry (Paytan et al., 2002); (2) hydrothermal barite that formed by the mixing of barium-rich hydrothermal fluids with seawater sulfate close to high-temperature vents (Kusakabe et al., 1990); (3) diagenetic barite occurring along diagenetic fronts at which barium- and/or hydrocarbon-rich fluids encounters with sulfate-bearing pore waters (Torres et al., 1996a, 1996b); (4) cold seep barite precipitating from cold-seep fluids containing voluminous hydrocarbons and barium near the sediment-water interface along continental margins (Naehr et al., 2000; Torres et al, 2003; Aloisi et al., 2004; Feng and Roberts, 2011). When Ba/CH_4-rich seep fluids migrate from the sulfate-depleted methanogenesis zone to the sediment-water interface through faults or lateral tectonic compression, the diagenetic barite formed in the sulfate-methane transition zone (SMTZ) could turn into the cold seep barite instead (Torres et al., 2003; Castellini et al., 2006; Zhou et al., 2016).

The Taxkorgan area situated at the junction of the Western Kunlun orogenic belt and Pamir Plateau (Fig.1) hosted a potential metallogenic condition because of a long-term complicated tectonic evolution. In the past two decades, a number of large-scale iron deposits (e.g., Zankan, Laobing, Yelike) have been discovered in this area (Fig. 1c), and it is thus considered as an important iron prospecting target in Xinjiang province. Despite extensive geological and geochemical studies on these iron deposits in recent years, a few key issues, involving the genetic type, still remain controversial. A group of workers attributed them to Precambrian BIF-type (Chen et al., 2011; Feng et al., 2011; Li et al., 2015), whereas others suggest a marine volcanic sedimentary origin (Yan et al., 2012; Huang, 2014). Recently, Zheng et al. (2016) argued that the Kalaizi deposit should be a SEDEX Fe–Ba deposit. By comparing with various types of iron deposits around the world, Yan et al. (2012) proposed a new type (Pamir-type) for iron deposits in the Taxkorgan area. However, it is a little bit of arbitrary and lacks a regional perspective because of their study focusing only on the geological and geochemical features of the Laobing iron deposit.

Recently, a large-scale Fe–Ba deposit named Kalaizi was uncovered to the east of Laobing deposit by No. 2 Geological Party of Xinjiang Bureau of Geology and Mineral Resources (Fig. 1c). By comparison with other iron deposits, this deposit

owns an extra ca. 20 Mt barite ore reserves and has significant implications for regional Ba prospecting. However, so far, several intriguing problems, such as the genetic relationship among the sulfate, sulfide, and carbonate minerals, the source of barium, and the ore-forming mechanism of this Fe–Ba deposit are still unclear. In this regard, the magnetite–barite, anhydrite–sulfide, and dolomite–magnetite ores in this deposit are the main research objects. A systematic field geological investigation and petrological observations, coupled with trace element and S–C–O–Sr isotopic analyses of individual minerals were conducted. Our ultimate aim is to provide useful clues for understanding the genesis of Kalaizi barite deposit and deciphering the corresponding ore-forming mechanism.

2. Regional geology

The western Kunlun orogenic belt, extending from the southern margin of the Tarim Craton to the northern margin of the Tibet Plateau (Fig. 1a), is made up of four tectonic units (Fig. 1b; Pan, 2000; Wang, 2004; Zhang et al., 2007): the North Kunlun, South Kunlun, Taxkorgan–Tianshuihai, and Karakorum terranes, which are separated by early Palaeozoic Oytag–Kudi suture zone and Mesozoic Mazar–Kangxiwar and Karakorum faults (Pan, 2000; Mattern and Schneider, 2000; Xiao et al., 2002; Zhang et al., 2007). The Taxkorgan area is situated in the southwestern part of the Taxkorgan–Tianshuihai Terrane (Fig. 1b). It has a NW–SE trend defined by the Mazar–Kangxiwar and Karakorum faults.

All iron ore deposits in Taxkorgan occur in the metamorphosed volcano-sedimentary sequences of a previously defined “Paleoproterozoic Bulunkuole Group” (Fig. 1c). It consists of magnetite-bearing quartzite, meta-basalt, meta-greywacke, and marble (Ji et al., 2011), which have been subjected to regional greenschist- to lower amphibolite-facies metamorphism during 460–400 Ma and 240–200 Ma (Zhang et al., 2007). The overlying rocks show a fault contact relationship with the Bulunkuole Group and can be further divided into the Lower Silurian (Wenquangou Group) graptolite-bearing clastic and carbonate sedimentary

rocks with minor volcanic rocks, the Upper Carboniferous carbonate rocks, the Middle Permian clastic and carbonate sedimentary rocks with minor volcanic interlayers, and the Lower Cretaceous clastic and carbonate sedimentary rocks. Intrusive rocks with different ages are broadly exposed, including Permian, Triassic, Cretaceous, and Neogene granitic and granodioritic plutons (Fig. 1c).

So far, the depositional age of the Bulunkuole Group still remains uncertain. Based on the metamorphic grade, zircon U–Pb ages, whole-rock Rb–Sr isochron ages (2130–2700 Ma), and the presence of magnetite-bearing quartzites, the Bulunkuole Group was first considered as the Paleoproterozoic basement of the Karakorum stratigraphy (Li et al., 2008; Ji et al., 2011). Recently, however, a few workers argued against this conclusion by obtaining numerous zircon U–Pb ages of differing lithologies within this group, including: (1) detrital zircon U–Pb ages of 540–2200 Ma for two argillaceous gneiss samples from the southern section of Taxkorgan indicating that the Bulunkuole Group should be formed later than Neoproterozoic (Zhang et al., 2007); (2) the 521.3 Ma bimodal volcanic rocks in the Taaxi deposit (Gao et al., 2013); (3) detrital zircon U–Pb ages (510–540 Ma) from the meta-clastic sedimentary rocks associated with the Laobing anhydrite iron deposit (Yan et al., 2012); (4) A detailed zircon U–Pb isotopic study by Yang (2013) on different lithologies (meta-clastic rocks, granitic veins and pelitic granulite) in differing localities revealing that the Paleoproterozoic sequence does not exist in the Bulunkuole Group and that the Bulunkuole Group, to some extent, contains Neoproterozoic (706–558 Ma), early Paleozoic (ca. 515 Ma), and Permian rocks (251–221 Ma); (5) a LA–ICP–MS zircon U–Pb age (ca. 537.2 Ma) of meta-volcanic rocks (biotite plagiogneiss) interlayered with the Kalaizi deposit (Zheng et al., 2016).

Based on the above results, the “Paleoproterozoic Bulunkuole Group” has been substituted using the “undefined Paleoproterozoic to early Cambrian Bulunkuole Group” and needs to be revisited in the future (Zheng et al., 2016; Fig. 1c). It should be noted that this suite of Early Cambrian lithologies host most but not all of iron deposits, e.g., the Qikeerke, Yelike, Laobing, and Kalaizi deposits, and that they are characterized by the presence of anhydrite–magnetite and/or

anhydrite–barite–magnetite assemblages (Zhang et al., 2016; Zheng et al., 2016). Interestingly, the abundant sulfate minerals in Lower Cambrian sedimentary sequences indicate a change from Precambrian anoxic sulfate-poor oceans to Phanerozoic oxygenated sulfate-rich oceans (Jewell, 2000; Lyons et al., 2006). As newly recognized rock units, the relevant tectonic setting is still unclear. Several workers proposed an extensional tectonic setting for the West Kunlun and its adjacent region in the Early Palaeozoic (Pan, 2000; Jiang et al., 2000; Gao et al., 2013).

3. Deposit geology

The rocks exposed in the Kalaizi deposit are the Early Cambrian Bulunkuole Group consisting mainly of garnet-bearing two-mica quartz schist, two-mica quartz schist (meta-argillaceous sandstone), lenticular dolomitic marble, sulfurized albite quartzite, anhydrite with lesser amounts of biotite plagioclase gneiss (meta-felsic volcanic rocks), which have undergone greenschist-facies regional metamorphism (Fig. 2). As shown in the cross-section (Fig. 3), the No. II magnetite–barite ore body is closely associated and intercalated with quartz schists. They occur as monoclinic, with striking 110–145° and dipping at a moderate to steep angle of 41–79°. The secondary fractures are widely developed due to effects of the regional Taaxi and Kangxiwar faults. Intrusive rocks in this area are dominated by biotite granite and mafic dyke (Fig. 2). The former located in the northwest is slightly reddish, medium-grain, and consists predominantly of K-feldspar, quartz, plagioclase, and biotite; whereas the latter strikes NW with 2 to 2.5 km in length and occurs as intruding into the wall rocks.

The Kalaizi deposit has a barite ore reserve of ca. 20 Mt with an average grade of 43 wt % and an accompanying iron ore reserve of ca. 8 Mt with an average grade of 15–20 wt %. Other elements, such as Pb, Zn, and sulfur, are of little economic interest. The No. II principal ore body, 2 km in length and 50–200 m in width, contains all barite and consists of seven small ore lenses (Fig. 2). All the lenses are intercalated with quartz schists (Fig. 3, 4) and make Kalaizi become a unique Fe–Ba deposit

within regional sulfate-bearing iron deposits. Moreover, an anhydrite–sulfide ore body termed No. IIS_2 occurs in the hanging wall of No. II ore body and is only observed in drill holes (Fig. 3).

The typical ores are disseminated (Fig. 4d, 5e, 5g and 5h), or laminated (Fig. 4c, 5a, 5d), and or massive, with ore minerals composed dominantly of barite and magnetite with minor pyrite, sphalerite, and galena, while gangue minerals consisting mainly of quartz, dolomite, ankerite, muscovite, and biotite. Based on different mineral assemblages, four ore types can be identified. (1) Magnetite–barite ore, occurring only in No. II ore body, is characterized by alternating magnetite- and barite-rich layers with laminated to banded structures (Fig. 5a). It consists of 15–80% barite, 10–30% magnetite, 15–30% quartz, and 10–25% ankerite (Fig. 5b, 5c). (2) Dolomite–magnetite ore found in No. IV ore body generally has low iron content and is associated with dolomite marble. Magnetite minerals within it occur as sparse grains or constitute microlaminae (Fig. 5d, 5e). The main mineral compositions are 15–35% magnetite, 50–75% dolomite and 5–15% quartz (Fig. 5f). (3) Muscovite–quartz–magnetite ore, as one main ore type of No. I ore body, comprises 5–15% biotite, 20–35% muscovite, 30–45% quartz, and 15–35% magnetite (Fig. 5g). (4) Anhydrite–pyrite and anhydrite–galena–sphalerite ores (No. IIS_2 ore body, Fig. 3) located in the hanging wall of No. II ore body are subordinate but with specific significance for relevant genesis (see below). Anhydrite–pyrite ore consists of pyrite, anhydrite, quartz, and mica with disseminated or laminated texture, while the anhydrite–galena–sphalerite ore is composed of anhydrite, galena, and sphalerite (Fig. 5h, 5i). In places, secondary textures, e.g., disseminated, coarse-grained magnetite crystals (Fig. 5g) and tight folds (Fig. 5d) restricted to ores, are present due to the post-depositional metamorphism and deformation.

4. Samples and methods

In this study, laminated magnetite–barite ores from No. II ore body, disseminated anhydrite sulfide ores from No. IIS_2 ore body and disseminated to banded

dolomite–magnetite ores from No. IV ore body were sampled in representative drill holes. As mentioned above, the rocks in the Kalaizi deposit have undergone greenschist-facies metamorphism and thus the primary sulfur and oxygen isotopes should not be affected by low-grade metamorphism (Huston, 1999). All samples were crushed, rinsed with distilled water, dried, and sieved to 60–80 mesh. Barite, ankerite, and magnetite individual minerals were separated from laminated magnetite–barite ores, anhydrite, pyrite, and galena samples were separated from disseminated anhydrite–sulfide ores, and dolomites were separated from banded dolomite–magnetite ores. Then, geochemical and isotopic analyses, including trace element and S–C–O–Sr isotopic measurements were carried out at the Institute of Geology and Geophysics, Chinese Academy of Sciences (IGGCAS).

Trace element concentrations of the magnetite were analyzed with an inductively coupled plasma-mass spectrometer (ICP–MS) (Element, Finnigan MAT) using solution methods. The uncertainties in this analysis were less than ±5%. Sulfur isotopes of barite, anhydrite, and sulfide samples were measured with a Finnigan Delta–S mass spectrometer. Sulfate and sulfide samples were combusted in the presence of excess CuO in a vacuum to produce SO_2. These analyses are reported relative to the V–CDT international standard and have an analytical precision better than 0.2%. Oxygen isotope analyses from the same batch of barite and anhydrite powders were performed at a Finnigan MAT–262 mass spectrometer at IGGCAS. Moreover, carbon and oxygen stable isotopes of seven dolomite and ankerite samples were measured using a Finnigan MAT–262 mass spectrometer. Carbon isotope data are reported as $\delta^{13}C$ values, in ‰ notation relative to the VPDB standard; while the $\delta^{18}O$ values from sulfate and carbonate minerals are reported relative to the standard mean ocean water (VSMOW). The precision of analyses from MAT–262 mass spectrometer is better than 0.2‰ for both $\delta^{13}C$ and $\delta^{18}O$.

Barite samples were completely dissolved for strontium isotope ($^{87}Sr/^{86}Sr$) analysis by using Suprapur® sodium carbonate (Na_2CO_3) to avoid small-scale heterogeneities in barites (Breit et al., 1985), and the strontium was separated by standard ion-exchange chromatography. The $^{87}Sr/^{86}Sr$ compositions of the barite

samples were measured with an IsoProbe–T mass spectrometer. Repeated measurements on the NBS–987 Sr standard solution yielded a mean value of $^{87}Sr/^{86}Sr$ ratio of 0.710265 ± 0.000014 (2σ). Because of the extremely high Sr and low Rb concentrations in barite samples, the errors introduced by Na_2CO_3 and in situ ^{87}Rb decay for initial $^{87}Sr/^{86}Sr$ on the measurements should all be negligible (McCulloch, 1994; Griffith and Paytan, 2012).

5. Results

5.1. Trace elements

Four magnetite samples separated from magnetite–barite ores were analyzed for trace and rare earth elements (Table 1). Most LILEs (Large Ion Lithophile Elements; e.g., Rb, U, Li, and B) have concentrations less than 5 ppm except for Sr (4.16–79.18 ppm) and Ba (377.88–7117.21 ppm), whereas, the abundances of HFSEs (High field-strength Elements; e.g., Nb, Ta, Zr, Hf and Th) are lower due to relatively low partition coefficients in magnetite. The Post-Archean Australian Shale-normalized (PAAS; McLennan, 1989) REE patterns for these samples are displayed in Fig. 6. The absolute concentrations of total REE and Y (ΣREY) range from 5.79 to 37.82 ppm. A general LREE to HREE enrichment ($(La/Yb)_{PAAS}$ = 3.80–11.39), together with a pronounced Eu anomaly (Eu/Eu^*_{PAAS} = 2.02–11.03) and weak La (La/La^*_{PAAS} = 0.91–1.17) and Ce (Ce/Ce^*_{PAAS} = 0.82–0.97) anomalies is observed. Moreover, the Y anomaly (Y/Y^*_{PAAS} = 0.94–1.04) and concomitant Y/Ho ratios (27.19–33.38) are not high enough relative to modern seawater (Bau and Dulski, 1996).

5.2. Sulfur and oxygen isotopes

The $\delta^{34}S$ and $\delta^{18}O$ values of the barite and anhydrite samples from No. II ore body are given in Table 2. The barite samples have a narrow variation of $\delta^{34}S$ and $\delta^{18}O$ values, ranging from 39.3‰ to 42.8‰ and between 10.0‰ and 13.0‰, respectively. Similar trends are also found for the anhydrite samples ($\delta^{34}S$: 37.8‰ to 40.7‰; $\delta^{18}O$: 9.9‰ to 12.7‰). These $\delta^{34}S$ values are enriched but ^{18}O values

depleted when comparing to those of the Early Cambrian seawater sulfate ($\delta^{34}S$ = 33±3‰ and $\delta^{18}O$ = 14±1‰; Claypool et al., 1980; Kampschulte and Strauss, 2004; Goldberg et al., 2005). Meanwhile there is no correlation between $\delta^{34}S$ and $\delta^{18}O$ values for all sulfate samples studied herein (Fig. 7a).

The sulfur isotope compositions of the pyrite and galena samples selected from anhydrite–sulfide ores are also present in Table 2. Regardless of occurrences of pyrite samples, they own $\delta^{34}S$ values (16.3‰–23.5‰) nearly identical to that (18.4‰–19.5‰) of the galena samples.

5.3. Strontium isotopes

The $^{87}Sr/^{86}Sr$ values of the studied barites vary in a limited range from 0.7086 to 0.7097 (Table 2) and hence are more radiogenic than that of contemporary seawater (~0.7084–0.7086; Maloof et al., 2010; Li et al., 2013). In addition, no discernable co-variation is present between $^{87}Sr/^{86}Sr$ ratios and $\delta^{34}S$ values for these samples (Fig. 7c).

5.4. Carbonates carbon and oxygen isotopes

Carbonate minerals are recognized based on electron microprobe data (not shown). Due to the significant amounts of FeO in some carbonates, ankerite (chemical formula: $Ca(Mg_{0.42}Fe_{0.38}Mn_{0.20})(CO_3)_2$) is identified intergrown with barite and magnetite (Fig. 5b, 5c); whereas iron-poor carbonates (dolomite, $Ca(Mg_{0.77}Fe_{0.18}Mn_{0.05})(CO_3)_2$) are found coexisting with magnetite (Fig. 5f). In the plot of $\delta^{13}C$ vs. $\delta^{18}O$, there are clearly two clusters with respect to these carbonates (Fig. 7d). The $\delta^{13}C$ and $\delta^{18}O$ values of the dolomites span a range from -3.3‰ to -4.6‰ and 12.9‰ to 14.0‰, respectively, while the ankerite samples have distinct $\delta^{13}C$ values of -10.0‰ to -12.1‰ and similar $\delta^{18}O$ values of 12.7‰ to 14.0‰ (Table 2).

6. Discussion

6.1. Origin of magnetite

Previous studies show that a significant iron ore belt hosting almost all iron deposits, especially sulfate-bearing iron deposits, occurs exclusively in the Early Cambrian volcanic sedimentary sequences of Bulunkuole Group in the Taxkorgan area (Yan et al., 2012; Zhang et al., 2016; Zheng et al., 2016). Three typical deposits are located within this belt, namely, from southest to northwest, Kalaizi Fe–Ba, Laobing–Yelike anhydrite–iron, and Taaxi iron deposits (Fig. 1c). Given similar ages, occurrences, and mineral assemblages, magnetite in these deposits could be of a consistent origin.

Geological observations combined with the major and trace element analyses of iron ores which commonly contain anhydrite and are sampled from the Laobing iron deposit suggest a contribution from submarine hydrothermal fluids to the formation of magnetite (Yan et al., 2012; Chen et al., 2013). This is corroborated by a presence of appreciable polymetallic sulfides (e.g., pyrite, galena, and sphalerite) in No. IIS_2 anhydrite–sulfide ore body of the Kalaizi deposit (Fig. 3, 5h, and 5j). Generally, polymetallic sulfides are the typical index minerals of a submarine hydrothermal activity (Torres et al., 2003; Koski et al., 1988).

PAAS-normalized REE pattern is one of the most useful geochemical tools to recognize the role of hydrothermal activity (eg., Bau and Dulski, 1999; Planavsky et al., 2010; Fu et al., 2010). It is generally accepted that REE patterns of oxic and anoxic water are distinctly different from those of hydrothermal fluids (in hydrothermal fluids, there are generally LREE-enriched patterns, strong positive Eu anomalies, and suppressed chondritic Y/Ho values (~28), particularly for high-T hydrothermal fluids) (Alibo and Nozaki, 1999; Bau and Dulski, 1999). The REE patterns of four magnetite samples studied herein (Fig. 6) are characterized by enrichment of LREE relative to HREE, apparently positive Eu anomalies (Eu/Eu^*_{PAAS} = 2.08–10.27), as well as the absence of pronounced La, Ce and Y anomalies, thus suggesting a hydrothermal source (Alibo and Nozaki, 1999; Bau and Dulski, 1999; Bolhar and Van Kranendonk, 2007). This is also supported by low Y/Ho ratios (27.19–33.38). Taken these above together, all characteristics indicate a hydrothermal origin for magnetite in the Kalaizi deposit.

6.2. Genesis of barite, anhydrite and sulfide minerals

6.2.1. General characteristics of ancient stratiform barite

Recently, ancient stratiform barite deposits have received much consideration and are mainly divided into two genetic types: hydrothermal and modern cold seep origin. Torres et al. (2003) regarded the modern cold seep barites on continental margins as analogues to the Paleozoic stratiform, metal-deficient barite deposits. The remarkable features for cold seep-related barite deposits are summarized as follows (Torres et al., 2003; Koski and Hein, 2004; Johnson et al., 2004, 2009; Feng and Robert, 2011; Canet et al., 2014): (1) the barite crystals are well-defined, generally ranging from 0.02 to 0.7 mm, and occur as rosettes, nodular, or laminated textures; (2) fossil faunas are commonly observed; (3) sulfide mineralization is rare and organic-rich shales are closely associated; (4) a linear trend exists between S and O isotopes starting from a coeval seawater sulfate end member to another with higher values; (5) there may be a wide range of Sr isotopic values owning to multiple types of lithologies with which ore-forming fluids interact. In addition, direct evidence for specific contribution from methane to the formation of carbonates in these deposits is still ambiguous (Johnson et al., 2009; Peckmann and Thiel, 2004).

In contrast, hydrothermal barites occur as xenomorphic crosscutting tabular crystals, which commonly constitute rosettes with crystal size ranging between 0.02 to 0.07 mm (Paytan et al., 2002). Such barites are generally spatially associated with anhydrite and polymetallic sulfides (Koski et al., 1988; Torres et al., 2003). Moreover, $\delta^{34}S$ and $\delta^{18}O$ values of barites are nearly the same as those of coeval seawater sulfate and the $\delta^{18}O$ values tend to be lower due to the isotope exchange between sulfate and H_2O at the elevated temperatures during the formation of hydrothermal barite (Van Stempvoort and Krouse, 1994). In addition, Sr isotope ratios are commonly between coeval seawater and the Sr isotope ratios of pure hydrothermal fluids (Kusakabe et al., 1990; Paytan et al., 2002; Torres et al., 2003; Koski and Hein, 2004). However, these characteristics are not the absolute standards. Emsbo and Johnson (2004) argued that the absence of sulfides could not preclude a hydrothermal origin. The fluid inclusions,

multiple sulfur and O–Sr isotope studies of barites from JADE hydrothermal field (Central Okinawa Through), Southern California rifted Continental Borderland and Loki's Castle vent field indicated that bacterial sulfate reduction could also take place in hydrothermal systems (Lüders et al., 2001; Hein et al., 2007; Eickmann et al., 2014). Hence, some researchers proposed that both hydrothermal and biogenic processes could contribute to the formation of bedded barite deposits (Clark et al., 2004; Han et al., 2015).

6.2.2. Implications for the sulfur cycle

Generally, marine barites commonly occur as fine-grained crystals (generally smaller than 5 um; Paytan et al., 2002) and constitute a small deposit due to their low accumulation rate in modern ocean basins (Koski and Hein, 2004). Given a relatively large scale of the Kalaizi deposit, and coarse-grained barite crystals (0.2 mm–2.0 mm; Fig. 4d, 5b and 5c) despite a possible post-depositional metamorphic recrystallization, a marine origin is precluded. Because it is hard to discriminate between diagenetic and cold seep barite considering their similar geochemical signatures (Castellini et al., 2006; Zhou et al., 2016), so the most preferable genesis for Kalaizi barite is focused on hydrothermal or cold seep origin which is the same as the other Paleozoic stratiform barite deposits (Torres et al., 2003; Koski and Hein, 2004; Johnson et al., 2004, 2009; Canet et al., 2014).

The sulfur and oxygen isotope couples are commonly used to offer valuable insights into the sulfur cycle and provide further information on the sources of sulfur (Aharon and Fu, 2003; Johnson et al., 2004). Nearly consistent $\delta^{34}S$ and $\delta^{18}O$ values (Table 2 and Fig. 7a, b) for barite and anhydrite samples in the Kalaizi deposit indicate a similar source of sulfate. These $\delta^{34}S$ values are higher relative to coeval (Early Cambrian) seawater ($\delta^{34}S = 33 \pm 3‰$; Claypool et al., 1980; Kampschulte and Strauss, 2004), suggesting that the sulfur was derived from seawater and that sulfate in seawater had been partially reduced. In general, there are two patterns for sulfate reduction processes in modern seawater. One is thermal sulfate reduction (TSR), where significant sulfur isotope fractionation does not take place (Machel et al., 1995).

Hence, the corresponding $\delta^{34}S$ values of sulfates from hydrothermal systems are either compatible with or slightly greater (as much as 1 to 2 per mil) than that of contemporary seawater (Kusakabe et al., 1990; Paytan et al., 2002; Johnson et al., 2004). Given relatively higher values for the Kalaizi sulfates, they had not been subject to this reducing way. The other is bacterial sulfate reduction (BSR) (eq. (1)), which could at the same time generate an isotopically heavy reservoir of residual dissolved SO_4^{2-} and an isotopically light flux of S^{2-} that are transferred to the sediment pile (Hanor, 2000), owing to preferential breakage of ^{32}S–O bonds compared to ^{34}S–O bounds (Goldberg et al., 2006).

$$2CH_2O+SO_4^{2-} \rightarrow H_2S+2HCO_3^- \quad (1)$$

When in direct contact with metal ions (e.g., Fe, Ba, Ca), sulfate minerals would be deposited along with polymetallic sulfides. Considering that there is insignificant sulfur isotopic fractionation during precipitation (Fry et al., 1988), the resulting sulfide and sulfate minerals can retain the S isotopic compositions of H_2S and SO_4^{2-}. Therefore, there is obviously positive S isotope fractionation between sulfate and sulfide minerals with a general fractionation of 15–60‰ (Ohmoto and Rye, 1979). Moreover, continuous removal of H_2S via the precipitation of metal sulfide under sulfate limited conditions (close system) would enrich the residual sulfate in $\delta^{34}S$ as the reaction proceeds (Johnson et al., 2004; Goldberg et al., 2006). This is also confirmed by relatively lower $\delta^{34}S$ values of pyrite and galena samples (16.3–23.5‰) coexisting with anhydrite and average $\Delta^{34}S_{Sulfate–Sulfide}$ value (the deviation of $\delta^{34}S$ value of sulfate mineral from associated sulfide) of 21‰ in the Kalaizi deposit (Table 2, Fig. 7b). It is unlikely that hydrothermal H_2S input would had a major influence on the precipitation of sulfides, since $\delta^{34}S$ values of the hydrothermal influx commonly lie around 0–3‰ (Kusakabe et al., 1990).

Theoretical and experimental studies both suggest that the kinetic effects of biological sulfate reduction generally produce a positive correlation between $\delta^{34}S$ and $\delta^{18}O$ values of sulfates (Aharon and Fu, 2000; Johnson et al., 2004). In other words, high $\delta^{34}S$ values of sulfates are accompanied by high $\delta^{18}O$ values. However, the $\delta^{18}O$ values of Kalaizi sulfates are lower than that of coeval seawater ($\delta^{18}O$=14±1‰;

Claypool et al., 1980; Goldberg et al., 2005) and no correlation is present between $\delta^{34}S$ and $\delta^{18}O$ (Fig. 7a), which are ascribed to either H_2S oxidation or S^0 disproportionation reactions that lead to the formation of sulfates (Böttcher et al, 2001; Böttcher and Thamdrup, 2001) or relatively high temperature (approximately 150°C) that is enough to result in an isotope exchange between sulfate and H_2O (Van Stempvoort and Krouse, 1994; Johnson et al., 2004). Given that sulfur isotopic fractionation during re-oxidation of H_2S or S^0 disproportionation is negligible (Fry et al., 1988), it would not be used to account for higher $\delta^{34}S$ values of sulfates in the Kalaizi deposit. Therefore, the latter process is reasonable.

Notably, isotopic fractionation is likely to be strongly influenced by sulfate reduction rate. In a restricted pore fluid system with limited sulfate input from the overlying seawater, the $\delta^{34}S$ and $\delta^{18}O$ values of barites are gradually increased due to the progressive and efficient bacterial sulfate reduction occurring below the water-sediment interface. In contrast, because of the slower bacterial sulfate reduction rate in an open system, barite with lower $\delta^{34}S$ and $\delta^{18}O$ values is possibly precipitated above or at the water-sediment interface with a continuous supply of sulfate that leads to inefficient bacterial sulfate reduction (Wang and Li, 1991; Aharon and Fu, 2000, 2003; Feng and Robert, 2011). In addition, Feng and Robert (2011) also emphasized that reduction of up to 94% of the seawater sulfate could generate barite with the most positive $\delta^{34}S$ values, while lower $\delta^{34}S$ values of barites are attributed to the low extent of seawater sulfate reduction in an open system. For the studied barite and anhydrite minerals, no more than 25% of the seawater sulfate may have been reduced to form the sulfate minerals with centralized $\delta^{34}S$ values of 37.8‰ to 42.8‰ based on the Rayleigh fractional model (Aharon and Fu, 2000). In consideration of the $\Delta^{34}S_{Sulfate-Sulfide}$ values (average value of 21‰) at the same time, Kalaizi sulfate and sulfide minerals should form in a semi-closed marine environment accompanied with medium bacterial sulfate reduction rate.

6.2.3. Source of barium

Strontium is readily incorporated into the crystal structure of barite once it

formed, making strontium isotopic signatures preserve in barite and hence become a useful proxy to trace the source of Sr and coherent Ba for barite formation (Hanor, 2000). Generally, strontium isotopic compositions of seawater are controlled by two potential sources: continental weathering run-off with radiogenic Sr and hydrothermal fluids with low $^{87}Sr/^{86}Sr$ values (Paytan et al., 2002). Moreover, hydrothermal barites with significant negative $\Delta^{87}Sr/^{86}Sr$ values (the deviations of $^{87}Sr/^{86}Sr$ ratios from coeval seawater) indicate a nonradiogenic source for Sr and Ba, which are deriving from leaching oceanic basalts (Kusakabe et al., 1990), whereas modern cold seep barites have $\Delta^{87}Sr/^{86}Sr$ values within ±0.002 (Torres et al., 2003; Griffith and Paytan, 2012). The $^{87}Sr/^{86}Sr$ ratios of seven Kalaizi barite samples range from 0.7086 to 0.7097 (Fig. 7d), which are higher (within ±0.0013) than those of the Early Cambrian seawater (~0.7084–0.7086; Maloof et al., 2010; Li et al., 2013). These imply that Sr and Ba for Kalaizi barites were derived from the penecontemporaneous seawater modified by more radiogenic terrigenous sediments and that the Kalaizi deposit could be a cold seep-related barite deposit.

6.3. Genesis of carbonates

Carbonates within the Kalaizi ores can be divided into two types: dolomite intergrown with magnetite (Fig. 5f) and ankerite coexisting with barite and magnetite (Fig. 5b and 5c), which are just consistent with their differing carbon but similar oxygen isotopic signatures (Fig. 7d). The ankerite minerals are more depleted in $\delta^{13}C$ values (-10.0 to -12.1‰) compared to dolomite samples (-3.3 to -4.6‰). In general, there are a large number of carbon sources: (1) dissolved inorganic carbon (DIC) with the $\delta^{13}C$ value of 1‰ within seawater (Aharon et al., 1991); (2) a volcanic or mantle carbon (-3 to -8‰) (e.g., Deines, 1970; Perry et al., 1973; Des Marais and Moore, 1984); (3) organic matter (-20‰, Goñi et al., 1998); (4) methane (-25 to -50‰, Peckmann and Thiel, 2004) and non-methane hydrocarbons (-27‰, Kennicutt et al., 1988). It is noted that coupling the reduction of sulfate minerals to the oxidation of organic matter (eq. 1 above) could provide the light carbon isotopic values of carbonate minerals associated with sulfates. Therefore, the relatively lower carbonate

isotopic signature of ankerite studied here could have been derived exclusively from organically derived CO_2 mixing with a small amount of normal marine water. However, the light carbon of iron-poor dolomite instead has a likely hydrothermal origin because hydrothermal water circulating through older volcanic rocks may be slightly depleted in ^{13}C relative to seawater. This is also borne out by their close association with magnetite that records a hydrothermal contribution.

6.4. Genetic model

Maynard et al. (1995) divided barite deposits into continental margin type and intracratonic rift type in terms of tectonic settings where they were deposited. Lower radiogenic strontium isotopic values compared to the contemporaneous seawater are typical of barites deposited on the continental margin where little Pb or Zn can be observed associated spatially with these barites. By contrast, the latter type is characterized by higher strontium isotopes relative to coeval seawater and presence of a certain amounts of Pb or Zn sulfides, which are consistent with features of the Kalaizi deposit, implying that it should be formed in a rift. This is also corroborated by the existence of Early Cambrian bimodal volcanic rocks (521.3±3.3Ma, Gao et al., 2013) in the Taaxi iron deposit (Fig. 1c). Moreover, the slight higher $\delta^{34}S$ values of the sulfate minerals in the Kalaizi deposit compared to the coeval seawater due to the medium sulfate reduction rate suggest that they precipitated likely in a semi-restricted system. These relevant geochemical features of the Kalaizi sulfates are comparable with those of modern cold seep barites, further implying a cold seep origin. However, detailed comparison revealed a difference with regard to the occurrence of magnetite coexisting with sulfates, clearly indicating a hydrothermal imprint during diagenesis. This is further confirmed by lower $\delta^{18}O$ values of all sulfate samples and the presence of sulfide minerals (e.g., galena, sphalerite, and pyrite) in the Kalaizi deposit.

Importantly, barite hardly coexists with anhydrite in the Kalaizi deposit. It is commonly accepted that precipitation of anhydrite could only occur when the Ba^{2+} is completely consumed in terms of a system containing SO_4^{2-}, Ba, and Ca, as shown in the phase diagram reported by Maynard and Okita (1991) (Fig. 8a). Based on

diagrams illustrating the stability regions of Fe–S–O minerals proposed by Huston and Logan (2004), it is possible that magnetite is only stable under a reduced condition ($\Sigma SO_4/\Sigma H_2S < 10^{-2.5}$ and $\Sigma S_{Ancient\ seawater}/\Sigma S_{Modern\ seawater} < 10^{-5}$ at 25°C), and the barite deposition indicates a relatively oxidized condition ($\Sigma SO_4/\Sigma H_2S > 10^{-2.5}$ and $\Sigma S_{Ancient\ seawater}/\Sigma S_{Modern\ seawater} > 10^{-2.5}$ at 25°C). It is worth noting that as the temperature increases, the stable fields of barite and magnetite expand and likely overlap between 100 and 200°C, implying that the coexistence of barite and magnetite in Kalaizi (Fig. 5d, e) could occur under a relatively high-T condition.

In modern cold seeps, pore water sulfate can be consumed not only by oxidation of organic carbon (eq. 1 above), but also by anaerobic oxidation of methane (AOM, eq. (2), e.g, Boetius et al., 2000; Knittel and Boetius, 2009):

$$CH_4 + SO_4^{2-} \rightarrow HS^- + HCO_3^- + H_2O \qquad (2)$$

Below the water-sediment interface, the seawater sulfate is gradually reduced by bacterial sulfate reduction with the burial depth increasing (Goldhaber and Kaplan, 1980; Jørgensen et al., 2001). Once pore water sulfate has been consumed completely, continuous degradation of residual organic matter would lead to the generation of methane due to the methanogenic bacteria (Boetius et al., 2000; Knittel and Boetius, 2009). Because of the low solubility, barite can exist stably with the presence of dissolved residual sulfate in sulfate reduction zone (SRZ) and will be dissolved by AOM under the sulfate-depleted methanogenesis zone, which results in high barium concentration in pore water (Torres et al., 1996b; Riedinger et al, 2006). So the transition zone from SRZ to the sulfate-depleted methanogenesis zone called sulfate-methane transition zone (SMTZ) is vital for the barium cycle (Torres et al., 1996a; Dickens, 2001; Aloisi et al., 2004; Zhou et al., 2015). By analogy with cold seep barite, barium was likely to derive from the dissolution of marine barite that was modified by terrigenous sediments in Kalaizi. As Ba/CH_4-rich fluids that released from AOM discharged at the sediment-water interface through tectonic processes, cold seep or Kalaizi barite would reprecipitate when interacting with residual sulfate from SRZ (Torres et al., 1996a; Castellini et al., 2006; Zhou et al., 2016). However, the relevant evidence for the presence of CH_4 is still a problem in this study. This may

be attributed to a fast fluid seepage condition which is indicated by the slightly higher $\delta^{34}S$ values of the Kalaizi sulfate minerals due to the medium bacterial sulfate reduction rate (Feng and Robert, 2011), because CH_4 could lost from the vent site as a benthic flux in high seepage conditions (Aloisi et al., 2004; Johnson et al., 2009).

Above all, the corresponding ore-forming mechanism of the Kalaizi deposit is shown in Fig. 9 and summarized as follows. In the Early Cambrian semi-restricted and rifted basinal situation, the process of barite mineralization experienced four steps, including input of marine barite flux, dissolution of marine barite, migration of Ba/CH_4-rich seep fluids, and formation of Kalaizi barite (Fig. 9). At the same time, bacterial sulfate reduction in the sulfate reduction zone resulted in the accumulation of an abundant H_2S, SO_4^{2-}, and HCO_3^- at the shallower depth below sediment-water interface. Kalaizi anhydrite precipitated subsequently after barium was consumed. It should be noted that the lower water column likely contains a certain amount of hydrothermal-derived Pb, Zn, and Fe. As a consequence, such diverse mineral assemblages (sulfides, magnetite, and sulfates) observed within the Kalaizi Fe–Ba deposit would be produced under specific conditions.

7. Conclusions

Based on the field investigation and detailed geochemical analyses, the Kalaizi Fe–Ba deposit is proposed to be a cold seep-related deposit imprinted by hydrothermal fluids. Specifically, the slightly higher $\delta^{34}S$ values of sulfates relative to contemporaneous seawater, coupled with pronounced negative $\delta^{13}C$ values of ankerite samples, suggest an involvement of moderately efficient bacterial sulfate reduction under the presence of organic matter in a semi-restricted basinal environment. Moreover, strontium isotope data imply a continental contribution to the solutes (Ba). In comparison with typical cold seep barites, the occurrence of sulfides (pyrite, galena and sphalerite) and magnetite and relevant geochemical signatures clearly indicate a strong hydrothermal role in the formation of this deposit.

Acknowledgments

This research was financially supported by the National Natural Science Foundation of China (Grant NO. 41372100) and National 305 Project (Grant NO. 2015BAB05B02). We would like to thank Haicai Wu, Fubao He and other geological engineers from the NO.2 Geological Party, Xinjiang Bureau of Geology and Mineral Resources for their assistance during field work. We appreciate the technical support in lab work provided by Lianjun Feng (sulfur, carbon and oxygen isotopes), Chaofeng Li (strontium isotope) and Wenjun Li (trace element analyses). We also thank Xiqiang Zhou for his guidance in the dissolution of barite for Sr isotope analysis.

References

Aharon, P., Graber, E.R., Roberts, H.H., 1991. Detection of hydrocarbon venting on the Gulf of Mexico sea floor from determinations of dissolved inorganic carbon and $\delta^{13}C$ of the water column overlying seeps. Gulf Coast Association of Geological Societies Transaction 41, 2–9.

Aharon, P., Fu, B.S., 2000. Microbial sulfate reduction rates and sulfur and oxygen isotope fractionations at oil and gas seeps in deepwater Gulf of Mexico. Geochimica et Cosmochimica Acta 64 (2), 233–246.

Aharon, P., Fu, B.S., 2003. Sulfur and oxygen isotopes of coeval sulfate-sulfide in pore fluids of cold seep sediments with sharp redox gradients. Chemical Geology 195 (1–4), 201–218.

Alibo, D.S., Nozaki, Y., 1999. Rare earth elements in seawater: particle association, shale-normalization, and Ce oxidation. Geochimmica et Cosmochimica Acta 63 (3–4), 363–372.

Aloisi, G., Wallmann, K., Bollwerk, S.M., Derkachev, A., Bohrmann, G., Suess, E., 2004. The effect of dissolved barium on biogeochemical processes at cold seeps. Geochimmica et Cosmochimica Acta 68 (8), 1735–1748.

Bishop, J.K.B., 1988. The barite-opal-organic carbon association in oceanic particulate matter. Nature 332, 341–343.

Bau, M., Dulski, P., 1996. Distribution of yttrium and rare-earth elements in the Penge and Kuruman iron-formations, Transvaal Supergroup, South Africa. Precambrian Research 79 (1–2), 37–55.

Bau, M., Dulski, P., 1999. Comparing yttrium and rare earths in hydrothermal fluids from the Mid-Atlantic Ridge: implications for Y and REE behaviour during near-vent mixing and for the Y/Ho ratio of Proterozoic seawater. Chemical Geology 155 (1–2), 77–90.

Bolhar, R., Van Kranendonk, M.J., 2007. A non-marine depositional setting for the northern Fortescue Group, Pilbara Craton, inferred from the trace element geochemistry of stromatolitic carbonates. Precambrian Research 155 (3–4), 229–250.

Boetius, A., Ravenschlag, L., Schubert, C.J., Rickert, D., Widdel, F., Gieseke, A., Amann, R., Jørgensen, B.B., Witte, U., Pfannkuche, O., 2000. A marine microbial consortium apparently mediating anaerobic oxidation of methane. Nature 407, 623–626.

Böttcher, M.E., Thamdrup, B., 2001. Anaerobic sulfide oxidation and stable isotope fractionation associated with bacterial sulfur disproportionation in the presence of MnO_2. Geochimmica et Cosmochimica Acta 65 (10), 1573–1581.

Böttcher, M.E., Thamdrup, B., Vennemann, T.W., 2001. Oxygen and sulfur isotope fractionation during anaerobic bacterial disproportionation of elemental sulfur. Geochimmica et Cosmochimica Acta 65 (10), 1601–1609.

Breit, G.N., Simmons, E.C., Goldhaber, M.B., 1985. Dissolution of barite for the analysis of strontium isotopes and other chemical and isotopic variations using aqueous sodium carbonate. Chemical Geology: Isotope Geoscience Section 52 (3–4), 333–336.

Canet, C., Anadón, P., González-Partida, E., Alfonso, P., Rajabi, A., Pérez-Segura, E., Alba-Aldave, L.A., 2014. Paleozoic bedded barite deposits from Sonora (NW Mexico): evidence for a hydrocarbon seep environment of formation. Ore Geology Reviews 56, 292–300.

Castellini, D.G., Dickens, G,R., Snyder, G.T., Ruppel, C.D., 2006. Barium cycling in

shallow sediment above active mud volcanoes in the Gulf of Mexico. Chemical Geology 226 (1): 1–30.

Chen, J.K., Yan, C.H., Zhang, W.S., Gao, T.C., Lv, X.H., Zhang, S.B., Hu, X.C., 2011. Geological characteristics and prospecting direction of the magnetite iron deposits in the Taxkorgan, Xinjiang. Geological Survey and Research 34 (3), 179–189 (in Chinese with Enligh abstract).

Chen, D.H., Wu, Y.Z., Li, W,M., Wang, X.A., Qiao, G,B., Zhao, X.J., 2013. Geological characteristics and genesis of the iron deposits in the Taxkorgan Area, West Kunlun. Geotectonica et Metallogeia 37 (4), 1–14 (in Chinese with Enligh abstract).

Clark, S.H.B., Poole, F.G., Wang, Z.C., 2004. Comparison of some sediment-hosted, stratiform barite deposits in China, the United States, and India. Ore Geology Review 24 (1), 85–101.

Claypool, G.E., Holser, W.T., Kaplan, I.R., Sakai, H., Zak, I., 1980. Age curves of sulfur and oxygen isotopes in marine sulfate and their mutual interpretation. Chemical Geology 28, 199–260.

Dehairs, F., Chesselet, R., Jedwab, J., 1980. Discrete suspended particles of barite and the barium cycle in the open ocean. Earth and Planetary Science Letters 49 (2), 529–550.

Deines, P., 1970. The carbon and oxygen isotopic composition of carbonates from the Oka carbonate complex, Quebec, Canada: Geochimica et Cosmochimica Acta 34 (11), 1199–1225.

Des Marais, D.J., Moore, J.G., 1984. Carbon and its isotopes in mid-oceanic basaltic glasses: Earth and Planetary Science Letters 69 (1), 43–57.

Dickens, G.R. 2001. Sulfate profiles and barium fronts in sediment on the Blake Ridge: present and past methane fluxes through a large gas hydrate reservoir. Geochimica et Cosmochimica Acta 65 (4), 529–543.

Emsbo, P., Johnson, C.A., 2004. Formation of modern and Paleozoic stratiform barite at cold methane seeps on continental margins: comment. Geology 32, e64.

Eickmann, B., Thorseth I.H., Peters, M., Strauss, H., Bröcker, M., Pedersen, R.B.,

2014. Barite in hydrothermal environments as a recorder of subseafloor processes: a multiple-isotope study from the Loki's Castle vent field. Geobiology 12 (4), 308–321.

Feng, C.R., Wu, H.C., Chen, Y., 2011. Geological characteristics and genesis of the Zankan iron deposit in Taxkorgan, Xinjiang. Geotectonica et Metalogenia 35 (3), 404–409 (in Chinese with Enligh abstract).

Feng, D., Roberts, H.H., 2011. Geochemical characteristics of the barite deposits at cold seeps from the northern Gulf of Mexico continental slope. Earth Planetary Science Letters 309 (1–2), 89–99.

Fry, B., Ruf, W., Gest, H., Hayes, J.M., 1988. Sulfur isotope effects associated with oxidation of sulfide by O_2 in aqueous solution. Chemical Geology 73 (3), 205–210.

Fu, X.G., Wang, J., Zeng, Y.H., Tan, F.W., Feng, X.L., 2010. REE geochemistry of marine oil shale from the Changshe Mountain area, northern Tibet, China. International Journal of Coal Geology 81 (3), 191–199.

Gao, X.F., Xiao, P.X., Kang, L., Zhu, H.P., Guo, L., Xi, R.G., Dong, Z.C., 2013. Origin of the volcanic rocks from the Ta'axi region, Taxkorgan Xinjiang and its geological significance. Earth Science: Journal of China University of Geosciences 38 (6), 1169–1182 (in Chinese with English abstract).

Goldberg, T., Poulton, S.W., Strauss, H., 2005. Sulphur and oxygen isotope signatures of late Neoproterozoic to early Cambrian sulphate, Yangtze Platform, China: diagenetic constraints and seawater evolution. Precambrian Research 137 (3), 223–241.

Goldberg, T., Mazumdar, A., Strauss, H., Shields, G., 2006. Insights from stable S and O isotopes into biogeochemical processes and genesis of Lower Cambrian barite–pyrite concretions of South China. Organic Geochemistry 37 (10), 1278–1288.

Goldhaber, M., Kaplan, I., 1980. Mechanisms of sulfur incorporation and isotope fractionation during early diagenesis in sediments of the Gulf of California. Marine Chemistry 9 (2): 95–143.

Goñi, M.A., Ruttenberg, K.C., Eglinton, T.I., 1998. A reassessment of the sources and importance of land-derived organic matter in surface sediments for the Gulf Mexico. Geochimical et Cosmochimica Acta 62 (18), 3055–3075.

Griffith, E.M., Paytan, A., 2012. Barite in the ocean-occurrence, geochemistry and palaeoceanographic applications. Sedimentology 59 (6), 1817–1835.

Han, S.C., Hu, K., Cao, J., Pan, J.Y., Xia, F., Wu, W.F., 2015. Origin of early Cambrian black-shale-hosted barite deposits in South China: Mineralogical and geochemical studies. Journal of Asian Earth Sciences 106, 79–94.

Hanor, J.S., 2000. Barite-celestine geochemistry and environments of formation. Review in Mineralogy Geochemistry 40 (1), 193–275.

Hein, J.R., Zierenberg, R.A., Maynard, J.B., Hannington, M.D., 2007. Barite-forming environments along a rifted continental margin, Southern California Borderland. Deep Sea Research Part II: Topical Studies in Oceanography 54 (11–13), 1327–1349.

Huang, C.Y., 2014. Geological characteristics and genesis of the iron ore deposit in the Bulunkuole Group, West Kunlun, Xinjiang. (Unpublished PhD thesis) Guangzhou institute of Geochemistry Chinese Academy of Sciences, Guangzhou, pp. 1–108 (in Chinese with English abstract).

Huston, D.L., 1999. Stable isotopes and their significance for understanding the genesis of volcanic-associated massive sulfide deposits: a review. In: Hannington, M.D., Barrie, C.T. (Eds.), Volcanic-Associated Massive Sulfide Deposits: Processes and Examples in Modern and Ancient Settings. Society of Economic Geology, pp. 157–179.

Huston, D.L., Logan, G.A., 2004. Barite, BIFs and bugs: evidence for the evolution of the Earth's early hydrosphere. Earth and Planetary Science Letters 220, 41–55.

Jewell, P.W., 2000. Bedded barite in the geologic record. In: Glenn, C.R., Prévôt-Lucas, L.J. (Eds.), Marine Authigenesis: From Global to Microbial. Society for Sedimentary Geology Special Publication 66, pp. 147–161.

Ji, W.H., Li, R.S., Chen, S.J., He, S.P., Zhao, Z.M., Bian, X.W., Zhu, H.P., Cui, J.G., Ren, J.G., 2011. The discovery of Palaeoproterozoic volcanic rocks in the

Bulunkuoler Group from the Tianshuihai Massif in Xinjiang of Northwest China and its geological significance. Science China Earth Sciences 54 (1), 61–72.

Jiang, C.F., Wang, Z.Q., Li, J.Y., 2000. Opening-Closing Tectonics of Central Orogenic Belt. Geological Publishing House, Beijing, pp. 1–154 (in Chinese).

Johnson, C.A., Kelley, K.D., Leach, D.L., 2004. Sulfur and oxygen isotopes in barite deposits of the western Brooks Range, Alaska, and implications for the origin of the Red Dog massive sulfide deposits. Economic Geology 99 (7), 1435–1448.

Johnson, C.A., Emsbo, P., Poole, F.G., Rye, R.O., 2009. Sulfur- and oxygen-isotopes in sediment-hosted stratiform barite deposits. Geochimica et Cosmochimica Acta 73 (1), 133–147.

Jørgensen, B.B., Weber, A., Zopfi, J., 2001. Sulfate reduction and anaerobic methane oxidation in Black Sea sediments. Deep Sea Research Part I: Oceanographic Research Papers 48 (9): 2097–2120.

Kampschulte, A., Strauss, H., 2004. The sulfur isotopic evolution of Phanerozoic seawater based on the analysis of structurally substituted sulfate in carbonates. Chemical Geology 204 (3–4), 255–286.

Kennicutt, M.C., Brooks, J.M., Denoux, G.J. 1988. Leakage of deep, reservoired petroleum to the near surface on the gulf of Mexico Continental slope. Marine Chemistry 24 (1), 39–59.

Knittel, K., Boetius, A., 2009. Anaerobic oxidation of methane: progress with an unknown process. Annual review of microbiology 63: 311–334.

Koski, R.A., Shanks, W.C., Bohrson, W.A., Oscarson, R.L., 1988. The composition of massive sulfide deposits from the sediment-covered floor of Escanaba trough, Gorda Ridge: Implications for depositional processes. Canadian Mineralogist 26, 655–673.

Koski, R. A., Hein, J. R., 2004. Stratiform barite deposits in the Roberts Mountains Allochthon, Nevada: a review of potential analogs in modern sea-floor environments. In: Bliss, J.D., Moyle, P.R., Long, K.R. (Eds.), Contributions to Industrial Minerals Research. U.S. Geological Survey Bulletin 2209–H, pp. 1–17. (http://pubs.usgs.gov/bul/b2209–h/).

Kusakabe, M., Mayeda, S., Nakamura, E., 1990. S, O and Sr isotope systematics of active vent materials from the Mariana backarc basin spreading-axis at 18°N. Earth and Planetary Science Letters 100 (1–3), 275–282.

Li, D., Ling, H.F., Shields-Zhou, G.A., Chen, X., Cremonese, L., Och, L., Thirlwall, M., Manning, C.J., 2013. Carbon and strontium isotope evolution of seawater across the Ediacaran-Cambrian transition: evidence from the Xiaotan section, NE Yunnan, South China. Precambrian Research 225, 128–147.

Li, R.S., Ji, W.H., Yang, Y.C., Yu, P.S., Zhao, Z.M., Chen, S.J., Meng, Y., Pan, X.P., Shi, B.D., Zhang, W.J., Li, X., Luo, C.Y., 2008. Geology of Kunlun Mountain and Adjacent Areas. Geological Publishing House, Beijing, pp. 1–5 (in Chinese).

Li, Z.Q., Zhang, L.C., Xue, C.J., Zheng, M.T., Hao, Y.H., Shi, Y.J., 2015. Geological and geochemical characteristics of Zankan iron deposit in the West Kunlun Mountains. Chinese Journal of Geology 50 (1), 100–117 (in Chinese with English abstract).

Lyons, T.W., Gellatly, A.M., McGoldrick, P.J., Kah, L.C., 2006. Proterozoic sedimentary exhalative (SEDEX) deposits and links to evolving global ocean chemistry. Geological Society of America Memoirs 198, 169–184.

Lüders, V., Pracejus, B., Halbach, P., 2001. Fluid inclusion and sulfur isotope studies in probable modern analogue Kuroko-type ores from the JADE hydrothermal field (Central Okinawa Trough, Japan). Chemical Geology 173 (1–3), 45–58.

Machel, H.G., Krouse, H.R., Sassen, R., 1995. Products and distinguishing criteria of bacterial and thermochemical sulfate reduction. Applied geochemistry 10 (4), 373–389.

Maloof, A.C., Porter, S.M., Moore, J.L., Dudás, F.Ö., Bowring, S.A., Higgins, J.A., Fike, D.A., Eddy, M.P., 2010. The earliest Cambrian record of animals and ocean geochemical change. Geological Society of America Bulletin 122 (11–12), 1731–1774.

Mattern, F., Schneider, W., 2000. Suturing of the Proto- and Paleo-Tethys oceans in the western Kunlun (Xinjiang, China). Journal of Asian Earth Sciences 18 (6), 637–650.

Maynard, J.B., Okita, P.M., 1991. Bedded barite deposits in the United States, Canada, Germany, and China: two major types based on tectonic setting. Economic Geology 86 (2), 364–376.

Maynard, J.B., Morton, J., Valdes-Nodarse, E.L., Diaz-Carmona, A., 1995. Sr isotopes of bedded barites: guide to distinguishing basins with Pb–Zn mineralization. Economic Geology 90 (7), 2058–2064.

McCulloch, M.T., 1994. Primitive $^{87}Sr/^{86}Sr$ from an Archean barite and conjecture on the Earth's age and origin. Earth and Planetary Science Letters 126 (1–3), 1–13.

McLennan, S.M., 1989. Rare earth elements in sedimentary rocks: Influence of provenance and sedimentary processes. In: Lipin, B.R., McKay, G.A. (Eds.), Geochemistry and Mineralogy of Rare Earth Elements. Reviews in Mineralogy and Geochemistry 21 (1), pp. 169–200.

Naehr, T.H., Stakes, D.S., Moore, W.S., 2000. Mass wasting, ephemeral fluid flow, and barite deposition on the California continental margin. Geology 28 (4), 315–318.

Ohmoto, H., Rye, R.O., 1979. Isotopes of sulphur and carbon, In: Barnes, H.L. (Eds.), Geochemistry of Hydrothermal Ore Deposits, second edition. John Wiley and Sons, New York, pp. 509–567.

Pan, Y.S., 2000. Geological Evolution of the Karakorum and Kunlun Mountains. Science Press, Beijing, pp. 21–98 (in Chinese).

Paytan, A., Mearon, S., Cobb, K., Kastner, M., 2002. Origin of marine barite deposits: Sr and S isotope characterization. Geology 30 (8), 747–750.

Peckmann, J., Thiel, V., 2004. Carbon cycling at ancient methane seeps. Chemical Geology 205 (3–4), 443–467.

Perry, E.C., Tan, F.C., Morey, G.B., 1973. Geology and stable isotope geochemistry of the Biwabik Iron Formation, northern Minnesota: Economic Geology 68 (7), 1110–1125.

Planavsky, N., Bekker, A., Rouxel, O.J., Kamber, B.S., Hofmann, A.W., Knudsen, A.,Lyons, T.W., 2010. Rare earth element and yttrium compositions of Archean and paleoproterozoic Fe formations revisited: new perspectives on the

significance and mechanisms of deposition. Geochimica et Cosmochimica Acta 74 (22), 6387–6405.

Riedinger, N., Kasten, S., Gröger, J., Franke, C., Pfeifer, K., 2006. Active and buried authigenic barite fronts in sediments from the Eastern Cape Basin. Earth and Planetary Science Letters 241 (3): 876–887.

Torres, M.E., Bohrmann, G., Suess, E., 1996a. Authigenic barites and fluxes of barium associated with fluid seeps in the Peru subduction zone. Earth and Planetary Science Letters 144 (3–4), 469–481.

Torres, M.E., Brumsack, H.J., Bohrmann, G., Emeis, K.C., 1996b. Barite fronts in continental margin sediments: a new look at barium remobilization in the zone of sulfate reduction and formation of heavy barites in diagenetic fronts. Chemical Geology 127 (1–3), 125–139.

Torres, M.E., Bohrmann, G., Dubé, T.E., Poole, F.G., 2003. Formation of modern and Paleozoic stratiform barite at cold methane seeps on continental margins. Geology 31 (10), 897–900.

Van Stempvoort, D.R., and Krouse, H.R., 1994. Controls of $\delta^{18}O$ in sulfate: Review of experimental data and application to specific environments. In: Alpers, C.N., Blowes, D.W., (eds.), Environmental geochemistry of sulfide oxidation. American Chemical Society, Washington, D.C., pp. 446–480.

Wang, Z.C., Li, G.Z., 1991. Barite and witherite deposits in Lower Cambrian shales of South China: stratigraphic distribution and geochemical characterization. Economic Geology 86 (2), 354–363.

Wang, Z.H., 2004. Tectonic evolution of the western Kunlun orogenic belt, western China. Journal of Asian Earth Sciences 24 (2), 153–161.

Xiao, W.J., Windley, B.F., Hao, J., Li, J.L., 2002. Arc-ophiolite obduction in the Western Kunlun Range (China): implications for the Paleozoic evolution of central Asia. Journal of the Geological Society 159 (5), 517–528.

Xu, L., Lehmann, B., Mao, J., Zheng, W., Ye, H., Li, H., 2016. Strontium, Sulfur, Carbon, and Oxygen Isotope Geochemistry of the Early Cambrian Strata-bound Barite and Witherite Deposits of the Qinling–Daba Region, Northern Margin of

the Yangtze Craton, China. Economic Geology 111 (3), 695–718.

Yan, C.H., Chen, C.J., Cao, X.Z., Zhang, W.S., Chen, J.K., Li, S.P., Liu, P.D., 2012. The discovery of the "Pamir-type" iron deposits in Taxkorgan area of Xinjiang and its geological significance. Geological Bulletin of China 31 (4), 549–557 (in Chinese with English abstract).

Yang, W.Q., 2013. The Indosinian metamorphism, magmatism and formation age of Bulunkuole rock group in Taxkorgan–Kangxiwar tectonic belt, Western Kunlun. (PhD thesis) Northwest University, Xi'an, pp. 1–128 (in Chinese with English abstract).

Zhang, C.L., Lu, S.N., Yu, H.F., Ye, H.M., 2007. Tectonic evolution of the Western Kunlun orogenic belt in northern Qinghai–Tibet Plateau: Evidence from zircon SHRIMP and LA–ICP–MS U–Pb geochronology. Science in China Series D: Earth Science. 50 (6), 825–835.

Zhang, L.C., Feng, J., Dong, L.H., Zhu, M.T., Zheng, M.T., Li, Z.Q. Hao, Y.H., Shi, Y.J., 2016. Deposit Types, Origin and Metallogenetic Regularity of Taxkorgan Iron Ore Belt in West Kunlun. Journal of Earth Sciences and Environment 38 (4), 427–443 (in Chinese with English abstract).

Zheng, M.T., Zhang, L.C., Zhu, M.T., Li, Z.Q., He, L.D., Shi, Y.J., Dong, L.H., Feng, J., 2016. Geological Characteristics, Formation age and Genesis of the Kalaizi Fe–Ba deposit in West Kunlun. Earth Science Frontiers 23(5): 252–265 (in Chinese with English abstract).

Zhou, X.Q., Chen, D.Z., Dong, S.F., Zhang, Y.Q., Guo, Z.H., Wei, H.Y., Yu, H., 2015. Diagenetic barite deposits in the Yurtus Formation in Tarim Basin, NW China: Implications for barium and sulfur cycling in the earliest Cambrian. Precambrian Research 263, 79–87.

Zhou, X.Q., Yu, H., Huang, T.Y., Zhang, L.Y., Zhang, G.J., Fu, Y., Chen, D.Z., 2016. Genentic Classification of Sedimentary Barites and Disscussion on the Origin of the Lower Cambrian Barite-rich Deposits in the Yangtze Block, South China. Acta Sedimentologica Sinica 34 (6), 1044–1056 (in Chinese with English abstract).

Zhou, Z.J., Tang, H.S., Chen, Y.J., Chen, Z.L., 2017. Trace elements of magnetite and iron isotopes of the Zankan iron deposit, westernmost Kunlun, China: A case study of seafloor hydrothermal iron deposits. Ore Geology Reviews 80: 1191–1205.

Highlights

(1) A Fe-Ba deposit formed in semi-closed basinal environment with medium bacterial sulfate reduction rate;

(2) Cold seep origin for Kalaizi barite overprinted by hydrothermal fluids;

(3) Barium was sourced from the dissolution of marine barite with a contribution from more radiogenic terrigenous sediments.

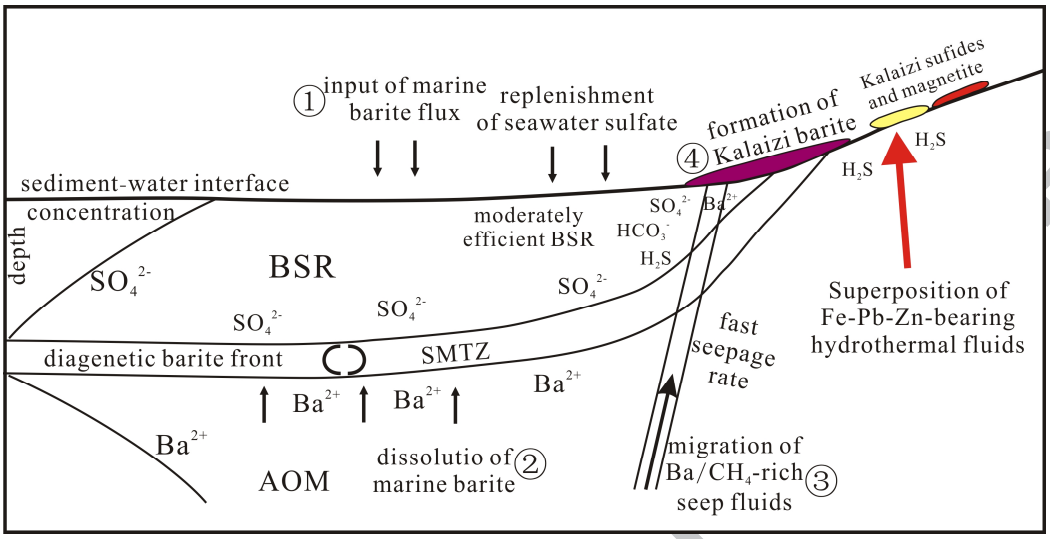

Figure captions

Fig. 1 (a) Simplified tectonic map of China, showing the location of the western Kunlun Orogenic Belt; (b) Tectonic subdivisions of the West Kunlun Orogen; (c) Geological sketch map and distribution of iron ore deposits and Fe–Ba deposit in Taxkorgan (Modified after Ji et al., 2011 and Zhou et al., 2017). The location of Fig. 2 is marked.

Fig. 2 Geological map of the Kalaizi Fe–Ba deposit (modified after No. 2 Geological Party of Xinjiang Bureau of Geology and Mineral Resources). The locations of cross-section line 65 and the drill hole No. ZK6103 (Fig. 3) are indicated.

Fig.3 (a) Geological cross-section, line 65 (see Fig. 2), in the Kalaizi Fe–Ba deposit (after No. 2 Geological Party of Xinjiang Bureau of Geology and Mineral Resources, the location of Fig. 4a is marked); (b) Lithostratigraphic column of drill hole No. ZK6103 (see Fig. 2).

Fig. 4 Field photographs of the Kalaizi Fe–Ba deposit. (a–b) Outcrop of the line 65 geological profile, the No. II_2 magnetite–barite ore body in conformable contact with the meta-argillaceous sandstone ((garnet-bearing) two-mica quartz schist) display the typical feature of sediment-hosted Fe–Ba deposit; (c–d) Magnetite–barite ores with laminated and disseminated structure.

Fig. 5 Photographs and photomicrographs of the Fe–Ba ores in the Kalaizi deposit. (a) Magnetite–barite ore from a drill hole, showing alternating cm-scale magnetite-rich and barite-rich banding; (b–c) Magnetite–barite ores which are composed of barite, magnetite, quartz and ankerite (Crossed polar); (d–e) Dolomite marbles that contain banded and disseminated magnetite; (f) Disseminated magnetite which is coexistence

with dolomite and quartz (Crossed polar); (g) Photomicrograph of muscovite–quartz–magnetite ore, displaying the disseminated structure and secondary enlargement of magnetite (plane polarized light); (h–i) Hand specimen and the corresponding photomicrograph (reflected light) of subhedral to anhedral pyrite, sphalerite and galena that coexist with anhydrite.
Abbreviations: Anh–anhydrite; Ank–ankerite; Bt–biotite; Brt–barite; Dol–dolomite; Ga–galena; Grt–garnet; Hb–hornblende; Ms–muscovite; Mt–magnetite; Py–pyrite; Q–quartz; Sp–sphalerite.

Fig. 6 PAAS-normalized REE+Y patterns of the Kalaizi magnetite, average high-T and low-T hydrothermal fluids, as well as average South Pacific seawater. The data of South Pacific seawater, high-T and low-T hydrothermal fluids are from Bolhar and Van Kranendonk (2007). The values of PAAS are after Mclennan (1989).

Fig. 7 (a) Sulfur and oxygen isotopic compositions of barite and anhydrite samples from the Kalaizi deposit. (b) Histogram which shows the overall distribution of $\delta^{34}S$ values in sulfate and sulfide minerals from the Kalaizi deposit. (c) Plot of $^{87}Sr/^{86}Sr$ and $\delta^{34}S$ values for the Kalaizi barite samples. (d) Plot of carbon and oxygen stable isotope compositions of the Kalaizi carbonates (dolomite and ankerite). Open squares indicate the isotopic compositions of the Early Cambrian seawater, which are derived from Claypool et al. (1980), Kampschulte and Strauss (2004), Goldberg et al. (2005) for sulfur and oxygen isotopes and from Maloof et al. (2010), Li et al. (2013) for $^{87}Sr/^{86}Sr$ ratio.

Fig. 8 (a) Phase diagrams showing stability fields for barite and anhydrite minerals in aqueous solution at 25°C and 1 atm under the condition of $a[Ca] = 10^{-2.63}$ and $a[CO_3] = 10^{-5.21}$, typical values of modern seawater (after Maynard and Okita, 1991); (b, c) $\Sigma SO_4/\Sigma H_2S$ versus total sulfur phase diagrams calculated at 25°C and 75°C under the condition of modern oceanic pH and salinity, showing the stability fields for Fe–Ba–S–O minerals (after Huston and Logan, 2004). Total sulfur concentrations are

normalized to the level in modern open ocean seawater.

Fig. 9 Proposed genetic model for the Kalaizi Fe–Ba deposit in a semi-closed rifted basin. The barium cyclic pattern is similar to modern cold seep barite. The process of the barite mineralization in Kalaizi involved four steps, including input of marine barite flux, dissolution of marine barite, migration of Ba-rich seep fluids, and formation of Kalaizi barite (modified from Torres et al., 2003; Castellini et al., 2006 and Zhou et al., 2016). Sulfate, sulfide, ankerite and magnetite minerals would precipitate when metal-bearing (lead, zinc and iron) hydrothermal fluids encountered with pore waters charged with SO_4^{2-}, H_2S and HCO_3^-.

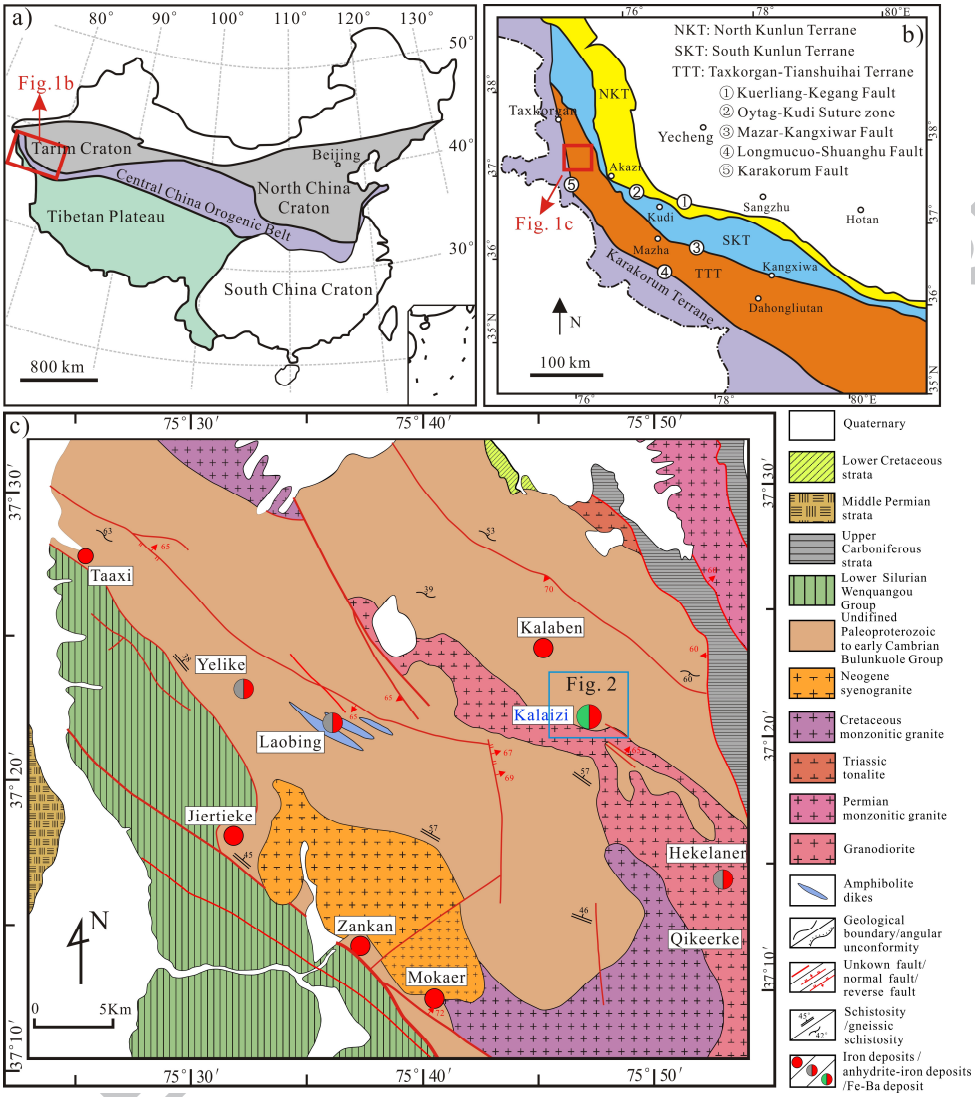

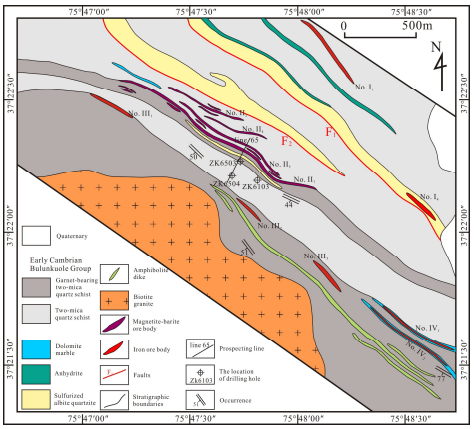

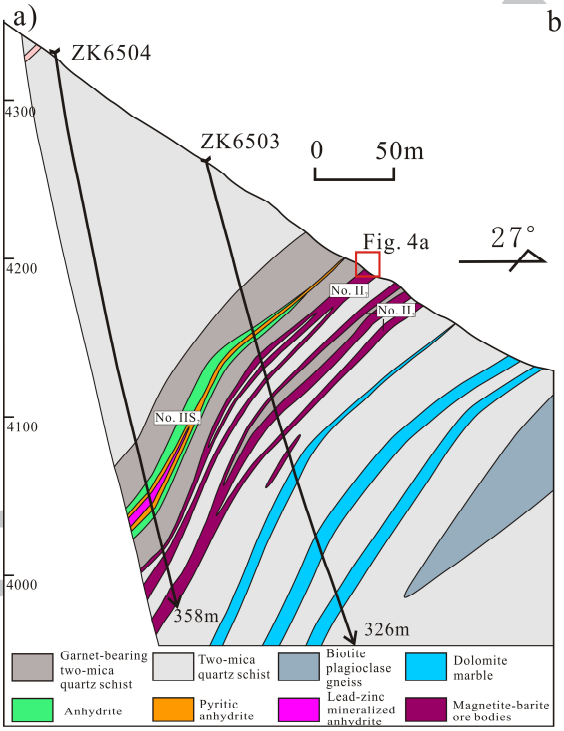

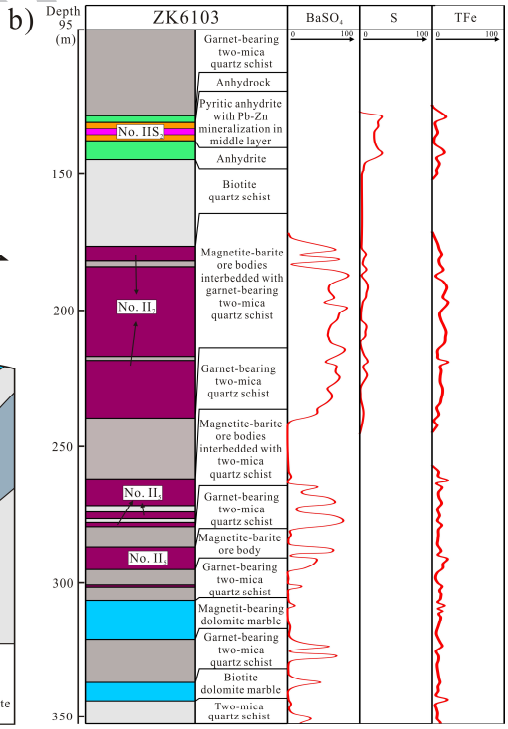

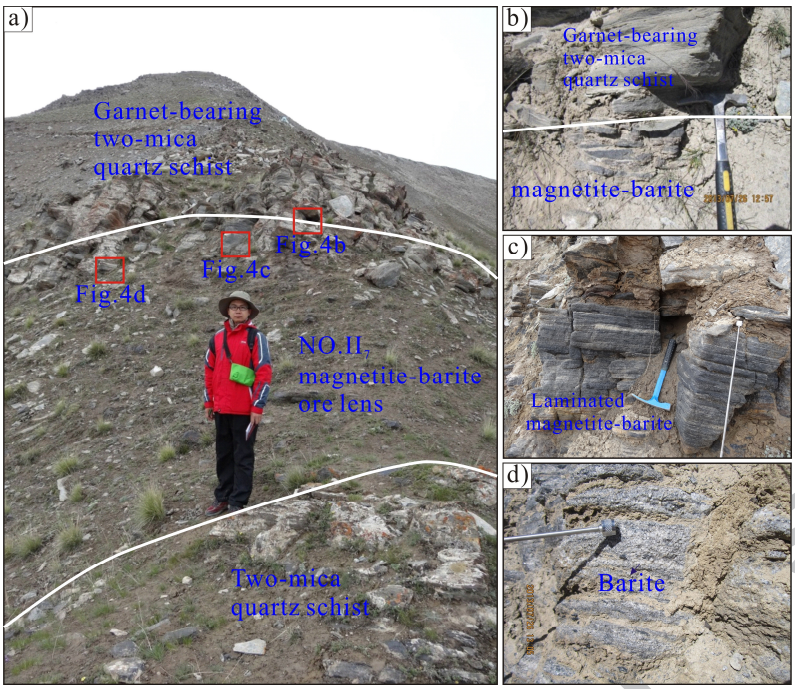

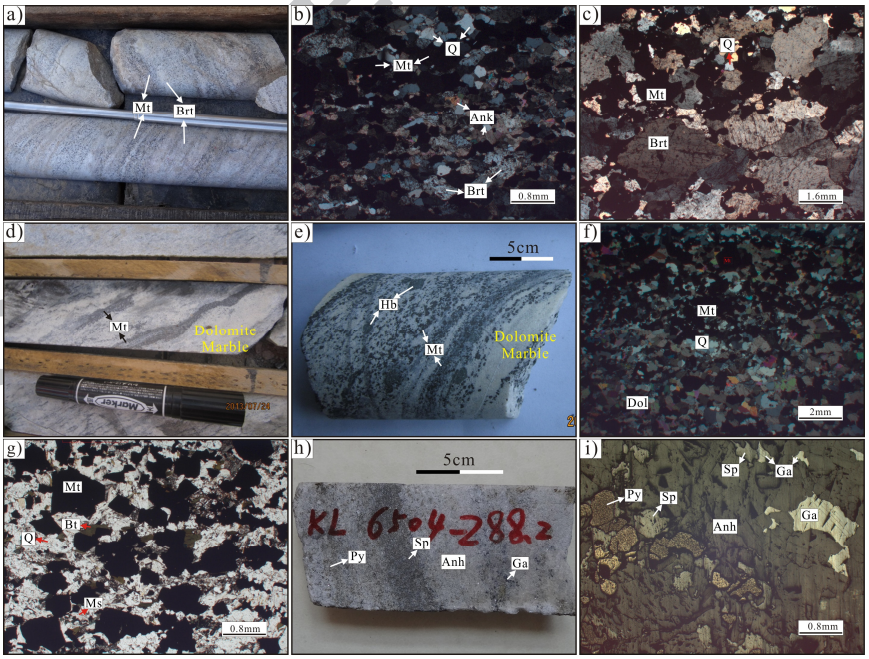

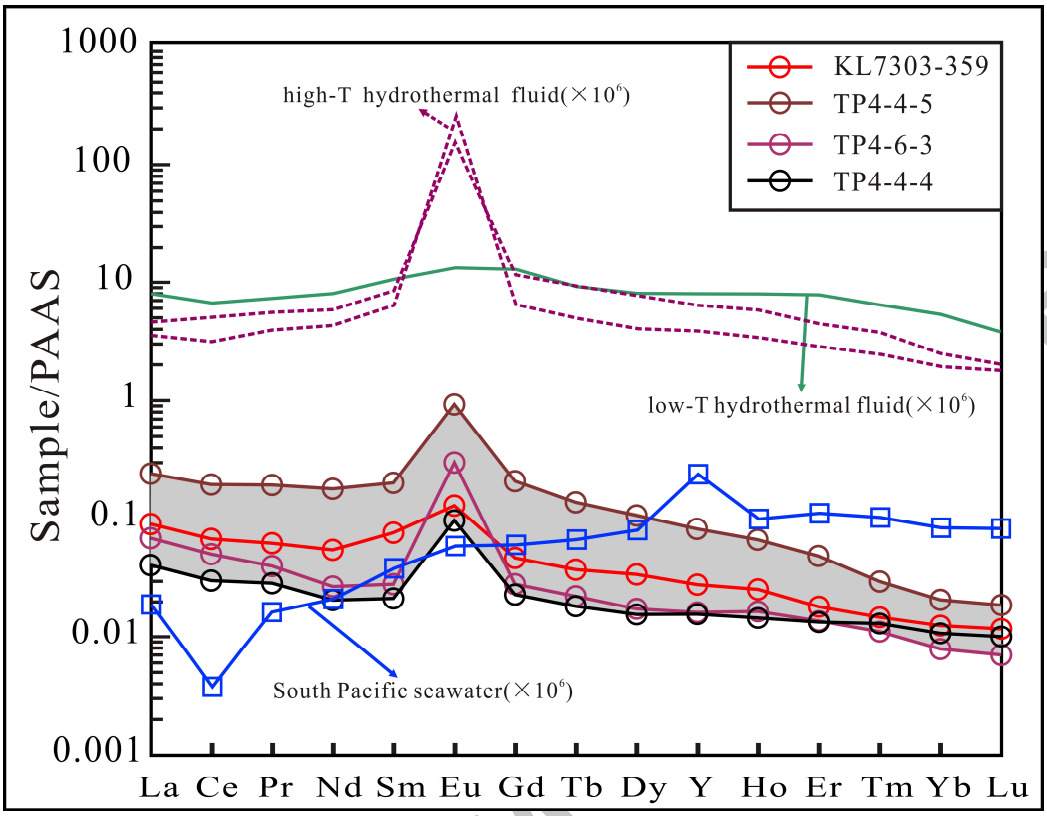

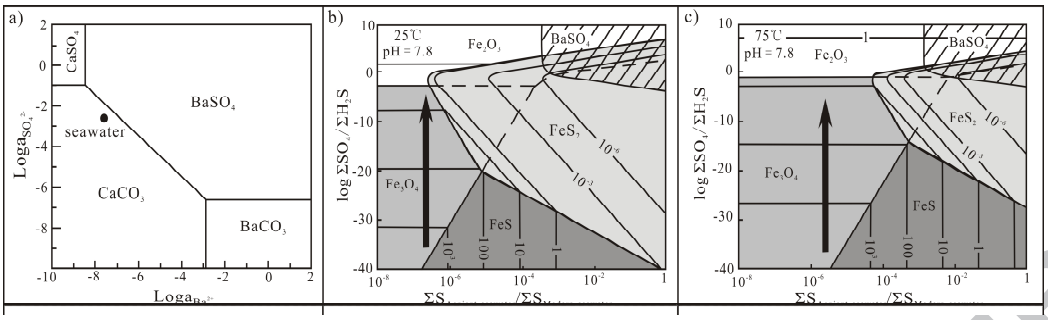

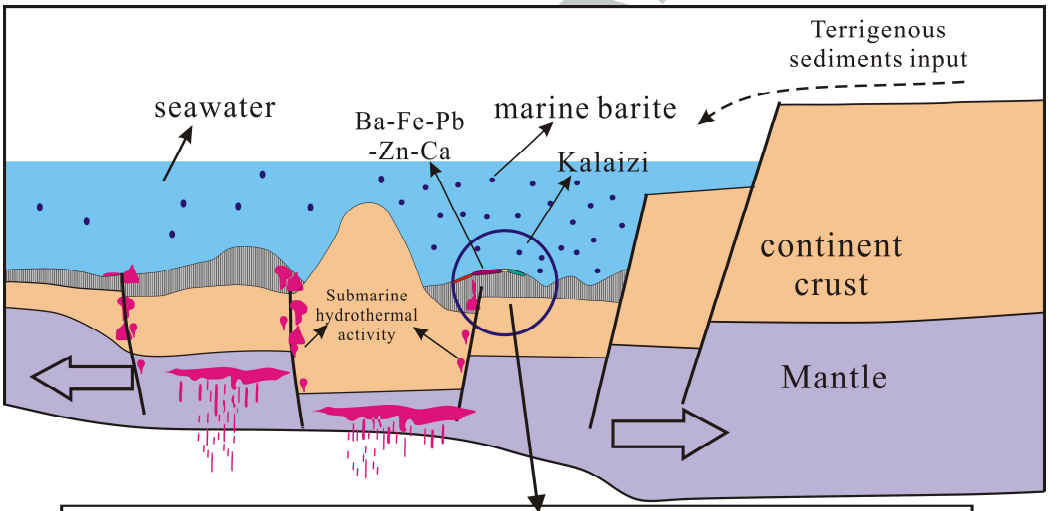

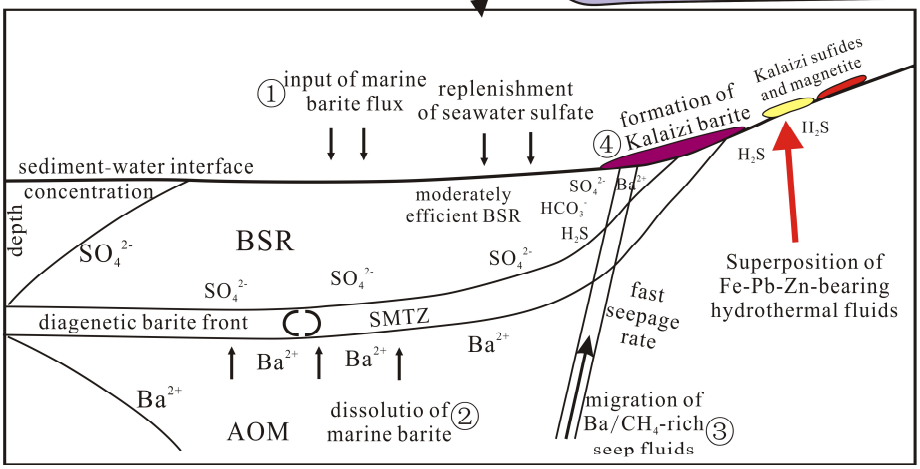

Table 1 Trace elements (ppm) of the magnetite samples separated from magnetite–barite ores in the Kalaizi deposit.

Sample	TP4-4-4	TP4-4-5	TP4-6-3	ZK7303-359	Sample	TP4-4-4	TP4-4-5	TP4-6-3	ZK7303-359
La	1.54	8.95	2.61	3.43	Eu/Eu^*_{PAAS}	4.72	5.06	11.03	2.02
Ce	2.38	15.2	3.96	5.33	Li	0.39	0.27	0.17	0.10
Pr	0.25	1.67	0.35	0.54	Be	0.01	0.01	0.00	0.04
Nd	0.70	5.95	0.90	1.83	Sc	0.09	0.01	0.00	0.04
Sm	0.12	1.09	0.16	0.42	V	27.57	10.22	1.63	15.84
Eu	0.10	0.96	0.31	0.14	Co	1.95	2.79	2.16	1.29
Gd	0.11	0.95	0.13	0.22	Cu	7.35	32.56	100.87	0.93
Tb	0.01	0.10	0.02	0.03	Zn	93.47	262.08	556.25	51.28
Dy	0.07	0.49	0.08	0.16	Ga	22.86	4.08	3.79	8.56
Y	0.42	2.17	0.44	0.75	Rb	0.04	0.81	0.56	0.46
Ho	0.01	0.07	0.02	0.03	Sr	4.16	79.18	47.94	35.20
Er	0.04	0.14	0.04	0.05	Zr	2.40	0.04	0.08	0.03
Tm	0.01	0.01	0.01	0.01	Nb	0.03	0.06	0.14	0.04
Yb	0.03	0.06	0.022	0.04	Cs	0.01	0.04	0.01	0.00
Lu	0.00	0.01	0.00	0.01	Ba	377.88	7117.21	3025.40	2299.90
ΣREE+Y	5.79	37.82	9.04	12.96	Hf	0.00	0.00	0.00	0.00
Y/Ho	30.00	33.38	27.19	29.88	Ta	0.02	0.00	0.04	0.00
$(La/Yb)_{PAAS}$	3.80	11.39	8.70	7.23	Tl	0.01	0.01	0.00	0.00
La/La^*_{PAAS}	0.91	1.08	1.05	1.17	Pb	208.12	40.30	46.60	4.05
Ce/Ce^*_{PAAS}	0.82	0.94	0.95	0.97	Th	0.39	0.01	0.01	0.01
Y/Y^*_{PAAS}	1.04	0.94	0.96	0.94	U	0.70	0.27	0.14	0.03

Note: $(La/Yb)_{PAAS} = La_{PAAS}/Yb_{PAAS}$, $La/La^*_{PAAS} = La_{PAAS}/(3Pr_{PAAS} - 2Nd_{PAAS})$, $Ce/Ce^*_{PAAS} = Ce_{PAAS}/(2Pr_{PAAS} - Nd_{PAAS})$ (Bolhar et al., 2004), $Eu/Eu^*_{PAAS} = Eu_{PAAS}/(0.67Sm_{PAAS} + 0.33Tb_{PAAS})$ (Bau and Dulski, 1996), $Y/Y^*_{PAAS} = 2Y_{PAAS}/(Dy_{PAAS} + Ho_{PAAS})$, PAAS values after Mclennan (1989).

Table 2 S–C–O–Sr isotopic analyses of the associated minerals in the Kalaizi deposit

Sample No.	ore types	mineral	$\delta^{34}S_{VCTD}$	$\delta^{13}C_{VPD}$	$\delta^{18}O_{VSMOW}$	$^{87}Sr/^{86}Sr$
TP4-4-4	Magnetite–barite ore	Barite	40.9*		13.0	0.7086
TP4-6-1	Magnetite–barite ore	Barite	41.3*		12.5	0.7087
TP4-6-2	Magnetite–barite ore	Barite	41.3*		10.8	0.7088
TP4-6-3	Magnetite–barite ore	Barite	42.8		10.8	0.7091
		Ankerite		-12.1	13.3	
KL7303-359	Magnetite–barite ore	Barite	39.3*		11.5	0.7091
		Ankerite		-11.8	14.0	
KL7303-357	Magnetite–barite ore	Barite	39.6		10.0	0.7088
		Ankerite		-10.0	12.7	
KL7303-350	Magnetite–barite ore	Barite	39.8		11.7	0.7097
		Ankerite		-11.8	13.3	
KL4105-157	Anhydrite–pyrite ore	Anhydrite	39.9*		10.7	
		Pyrite	23.5			
KL6504-288	Anhydrite–galena–sphalerite ores	Anhydrite	38.2		10.1	
		Pyrite	17.8			
		Galena	18.4			
KL6504-290	Anhydrite–galena–sphalerite ores	Anhydrite	40.5		11.3	
		Pyrite	16.3			
		Galena	19.5			
KL6504-291	Anhydrite–pyrite ore	Anhydrite	37.8		12.7	
		Pyrite	16.8			
KL4105-139	Anhydrite	Anhydrite	40.7*		9.9	
KL4105-182	Anhydrite	Anhydrite	39.5		12.0	
KL1202-160	Quartz–pyrite ore	Pyrite	17.0*			
KL1201-161	Quartz–pyrite ore	Pyrite	18.8*			
KL2501-368	Dolomite–magnetite ore	Dolomite		-4.2	14.0	
KL2501-371	Dolomite–magnetite ore	Dolomite		-3.3	13.8	
KL2501-381	Dolomite–magnetite ore	Dolomite		-4.6	12.9	

Note: $\delta^{34}S$ values marked by * are cited from Zheng et al., 2016